PAPER • OPEN ACCESS

Efficient state-symmetric beamsplitters and mirrors for atom interferometers using optimized pulses

View the article online for updates and enhancements.

Efficient state-symmetric beamsplitters and mirrors for atom interferometers using optimized pulses

Jack Saywell[1] , **Max Carey**[1] , **Nikolaos Dedes**[1], **Ilya Kuprov**[2] and **Tim Freegarde**[1,*]

[1] School of Physics & Astronomy, University of Southampton, Highfield, Southampton, SO17 1BJ, United Kingdom
[2] School of Chemistry, University of Southampton, Highfield, Southampton, SO17 1BJ, United Kingdom

E-mail: tim.freegarde@soton.ac.uk

CrossMark

Abstract
Atom interferometers that employ atoms in superpositions of different electronic states are sensitive to any noise that affects these superposed states differently. Resilience to such noise results from using superpositions where the atomic states differ in momentum only, but implementation of such 'state-symmetric' diffraction can lead to population loss into unwanted states and restricts the atomic velocity acceptance of the interferometer. In this paper, by varying the laser intensities and phases as functions of time, we present optimized pulses designed for use in state-symmetric interferometers that overcome these restrictions. We extend this optimization to multi-pulse sequences designed to increase the interferometer area and demonstrate significant improvements in the fringe visibility compared with sequences of $\pi/2$ and π pulses. We discuss the limits on the temperature of the atomic source required for efficient atomic diffraction and show how optimized pulse sequences enable efficient diffraction with considerably warmer clouds, hence reducing the need for velocity selection and increasing the measurement signal-to-noise ratio.

(Some figures may appear in colour only in the online journal)

1. Introduction

Atom interferometers [1, 2], many of which use sequences of laser pulses to diffract and interfere atomic matter-waves, are extremely sensitive inertial sensors and key components of quantum gravimeters [3–5], gradiometers [6–8], accelerometers [9], and gyroscopes [10–12]. The laser pulses in these devices typically effect multi-photon transitions between electronic ground levels in either Raman [13] or Bragg [14] diffraction regimes. Each regime has its advantages: Bragg pulses leave atoms in the same electronic state throughout, making the interferometer robust to magnetic field and laser phase noise between pulses [15] and, provided that the atomic sample is cold enough [16], are able to create large momentum superpositions in a single interaction. Raman pulses, meanwhile, are effective for much broader thermal distributions [17] and leave atoms in a superposition of different electronic states, sacrificing noise-resilience in favour of easy and rapid read-out [18].

Efforts have been made to combine the benefits of both approaches. Raman double-diffraction [17, 19, 20] utilizes simultaneous interaction between counter-propagating Raman beams to keep atoms in the same electronic state during the

interferometer, suppressing noise while still enabling electronic read-out. However, such interferometers suffer from losses to higher-order momentum states if the two-photon Rabi frequency is too high [21], in effect still limiting the technique to sub-recoil cloud temperatures, and are not extensible without fidelity loss [17] to the larger momentum transfer (and thus sensitivity) afforded by Bragg diffraction.

Another promising approach, introduced by Berg *et al* [22], replaces the single Raman $\pi/2$ (beamsplitter) and π (mirror) pulses with composite sequences of velocity-selective versions of these pulses in which the wave-vector direction is reversed. This state-symmetric Raman-based interferometer again benefits from the noise-resilience that comes from keeping atoms in the same electronic state between pulses and, unlike Bragg diffraction, still allows electronic-state detection while, unlike double-diffraction schemes, the interferometer fringe may be scanned by varying the laser phase during the final pulse and no additional frequency component in the Raman beams is required to compensate the Doppler shift in a gravimeter [20]. However, since the velocity-selective pulses added in the symmetric interferometer must address just one interferometer arm at any one time, the velocity acceptance of the interferometer is limited to sub-recoil distributions so that fewer atoms from a given source can participate in a measurement, lowering the signal-to-noise (SNR) ratio.

The limitations of all these techniques are fundamentally determined by the recoil momentum imparted by each pulsed interaction: the initial thermal distribution must be narrower than the momentum superposition created by the diffraction process. However, they are also limited by the efficiency of the laser pulses that perform the atomic diffraction. As we will see, the constraints put on the Rabi frequency by the requirement to discriminate between interferometer arms, combined with the large wings in the lineshape of typical π and $\pi/2$ pulses, mean that variations in atomic velocity can quickly reduce the pulse efficiency and hence measurement contrast, which falls particularly rapidly if extra pulses are added to increase the interferometer area. This makes field deployment of such devices a delicate balancing act between sensitivity and SNR ratio, making it common to filter out all but the coldest atoms and restrict the number of laser pulses.

Optimal control theory [23–29] may be adapted to design tailored laser pulses where the optical phase, frequency, and intensity are varied in time to create pulses with desired efficiency, frequency selectivity [30], and robustness to variations in frequency and coupling strength [31]. We have previously used optimal control to design individual robust Raman pulses for atom interferometers [32–35]. In this paper, we introduce a novel optimal control approach to the design of beamsplitter and mirror pulse sequences tailored for state-symmetric Raman interferometers where the $\pi/2$ and π pulses are replaced by alternatives in which the Raman laser phase and beam intensities vary smoothly with time. We show that these optimized sequences improve the velocity acceptance of state-symmetric interferometers significantly, reducing the need for velocity selection and consequently allowing more atoms to contribute to a measurement.

We also extend the state-symmetric interferometer design of Berg *et al* [22] to enable large-momentum-transfer (LMT) [36] by optimising extended sequences of robust pulses which minimize population loss to higher momentum states and demonstrate that the target momentum separation between the interferometer arms in a symmetric interferometer provides a theoretical upper limit on the velocity acceptance of the pulse sequence. Consequently, we show that by increasing the target momentum separation, optimized pulse sequences can simultaneously improve the intrinsic interferometer sensitivity and the velocity acceptance of symmetric Raman pulse interferometers.

2. State-symmetric interferometer sequences

In a Raman transition, two ground levels $|g\rangle$ and $|e\rangle$ (for example the hyperfine ground states $|5S_{1/2}, F = 2\rangle$ and $|5S_{1/2}, F = 3\rangle$ in ^{85}Rb) are coupled via two counter-propagating lasers with frequencies $\omega_1 = ck_1$ and $\omega_2 = ck_2$ whose frequency difference closely matches the splitting ω_{eg} between $|g\rangle$ and $|e\rangle$ [13]. Each laser is individually far-detuned from an upper intermediate level $|i\rangle$, which remains unpopulated, and Rabi flopping can occur between $|g\rangle$ and $|e\rangle$. Depending on the direction of each beam relative to the z-axis, an atom initially in the state $|g, p\rangle$ with momentum p in the z-direction may be coupled either to the state $|e, p + \hbar k_{\text{eff}}\rangle$ (the '$+\hbar k_{\text{eff}}$' or '+' transition) or to the state $|e, p - \hbar k_{\text{eff}}\rangle$ (the '$-\hbar k_{\text{eff}}$' or '−' transition), where the effective wave-number k_{eff} is given by $k_1 + k_2$ [17]. Both Raman transitions are depicted in figure 1, along with the direction of momentum transfer. The resonance condition for each Raman transition is given by [17]

$$\omega_1 - \omega_2 = \omega_{eg} + \delta^{\text{AC}} \pm \delta_{\text{D}} + \delta_{\text{R}}, \tag{1}$$

where δ^{AC} is the AC Stark shift and $\delta_{\text{R}} = \hbar k_{\text{eff}}^2/2m$ is the two-photon recoil shift ($\approx$15 kHz for ^{85}Rb) where m is the atomic mass. For convenience, we define the laser detuning $\delta_{\text{L}} \equiv \omega_1 - \omega_2 - \omega_{eg}$ and ignore the AC Stark shift as this may be compensated in practice [37]. $\delta_{\text{D}} \equiv k_{\text{eff}} v_z$ is the Doppler shift, and the $+$ and $-$ in equation (1) correspond to the $+\hbar k_{\text{eff}}$ and $-\hbar k_{\text{eff}}$ transitions, respectively. When the atom is initially at rest relative to the lasers, the resonance conditions for each transition are identical.

By swapping the propagation directions of the two Raman beams, hence reversing the effective wave-vector, the atom may be given successive two-photon recoil kicks to access a ladder of momentum states whose momenta differ by an integer number n of $\hbar k_{\text{eff}}$ [38]:

$$|g, p + n\hbar k_{\text{eff}}\rangle \equiv |g_n\rangle \tag{2}$$

$$|e, p + n\hbar k_{\text{eff}}\rangle \equiv |e_n\rangle. \tag{3}$$

For an atom resonant with a particular Raman transition ($-$ or $+$), Rabi flopping occurs at a frequency $\Omega_{\text{R}}^{\pm}$ between any two coupled states, leading to the concept of (rectangular) $\pi/2$ and π pulses, which are realized by keeping the relative laser phase ($\phi_{\text{L}} \equiv \phi_1 - \phi_2$, where ϕ_i is the phase of laser i)
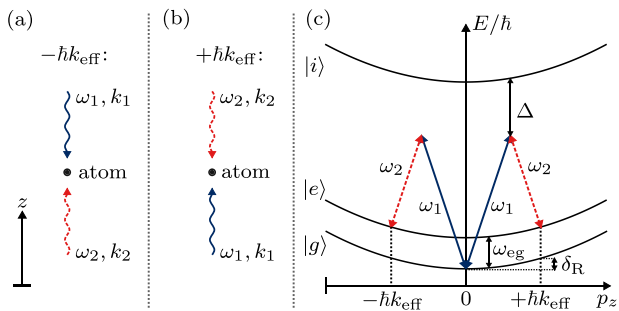
Figure 1. (a) and (b) Show the laser configurations for the $-\hbar k_{\text{eff}}$ and $+\hbar k_{\text{eff}}$ Raman transitions. (c) Depicts the energy–momentum diagram for each Raman transition, where individual photons from each laser are represented by diagonal lines. Two counter-propagating lasers with frequencies ω_1 and ω_2 induce Raman transitions between ground hyperfine levels $|g\rangle$ and $|e\rangle$. Both lasers are far-detuned by an amount Δ from an upper intermediate level $|i\rangle$, such that $\Delta \gg \omega_{\text{eg}}$.

and Rabi frequency fixed for durations of $\pi/2\Omega_R^{\pm}$ and $\pi/\Omega_R^{\pm}$, respectively. Given an atom initially in $|g\rangle$, a π pulse transfers population to the other coupled state and a $\pi/2$ pulse creates a superposition of the two. The efficiency, or fidelity of these processes is reduced if the resonance condition is not met, or if the pulse area (defined as the product of Rabi frequency and duration) is not precisely π or $\pi/2$. As the Rabi frequency is lowered (pulse length increased) for a single pulse, it becomes more narrowband: the range of detunings for which good fidelity is obtained reduces. Conversely, as the Rabi frequency is increased, it becomes more broadband.

Many Raman-based interferometers employ pulses in the Mach–Zehnder sequence, $\pi/2 - \pi - \pi/2$, where only a single effective wave-vector direction (e.g. $+\hbar k_{\text{eff}}$) is used throughout. Consequently, the atoms remain in superpositions of $|g_0\rangle$ and $|e_{+1}\rangle$ in the dwell times between the pulses. Extra pulses with alternating wave-vector directions can be used to enhance the momentum separation between these states forming a LMT interferometer [36]. This raises the intrinsic interferometer sensitivity (the measurement scale-factor) by increasing the area enclosed by the atomic wave-packets. However, as long as the atoms remain in different internal states during the dwell-times, the interferometer remains sensitive to fluctuations in the laser phase and magnetic field during these periods [22].

Figure 2(a) shows a space-time diagram for the state-symmetric atom interferometer pulse sequence first introduced by Berg *et al* [22]. For atoms initially prepared in the state $|g_0\rangle$, a $\pi/2$ pulse in the $+$ direction creates a superposition of $|g_0\rangle$ and $|e_{+1}\rangle$. A subsequent π pulse in the $-$ direction transfers atoms in $|g_0\rangle$ to $|e_{-1}\rangle$, resulting in a superposition in which atoms are in different momentum states but the same internal state—unlike a conventional Raman-based Mach–Zehnder interferometer.

Figure 2(b) shows the final transition probabilities following the symmetric beamsplitter sequence as a function of the initial atomic momentum (which manifests as a non-zero Doppler detuning). ^{85}Rb is the atomic species assumed for all the work in this paper and appendix A provides details
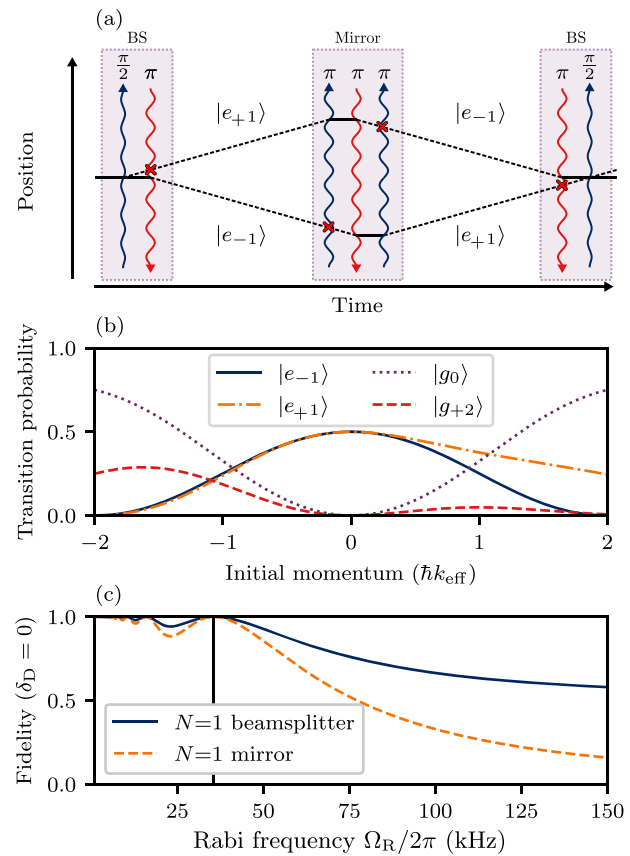

Figure 2. (a) Space-time diagram for a symmetric interferometer sequence. Beamsplitter and mirror interactions are composed of multiple Raman pulses, represented with vertical arrows. The arrows depict the direction of momentum transfer, where up corresponds to $+\hbar k_{\text{eff}}$ and down corresponds to $-\hbar k_{\text{eff}}$. Red crosses indicate where a pulse should *not* induce a transition. Atomic trajectories are solid (dashed) lines for atoms in the electronic state $|g\rangle$ ($|e\rangle$). (b) Shows the simulated transition probability corresponding to different possible states following the beamsplitter sequence in (a) for a range of initial atomic momenta $\pm 2\hbar k_{\text{eff}}$ simulated for $\Omega_R/2\pi = 35.6$ kHz. (c) Shows how the resonant fidelities of the beamsplitter and mirror sequence depend on the Rabi frequency, where the largest peak Rabi frequency 35.6 kHz is shown by a vertical line.

of the simulation method used to calculate state amplitudes. We see that for atoms with initial momenta much less than that imparted by a single two-photon recoil, the beamsplitter is efficient, and atoms are diffracted into an equal superposition of $|e_{+1}\rangle$ and $|e_{-1}\rangle$. However, unlike a conventional Raman beamsplitter (a single $\pi/2$ pulse), where the resonant fidelity of the pulse is unity for any combination of Rabi frequency and duration that yield a pulse area of $\pi/2$, increasing the Rabi frequency reduces the efficiency of the symmetric beamsplitter because the symmetric beamsplitter requires narrowband pulses.

In figure 2(c) we have plotted the resonant (zero initial atomic momentum) fidelity of the symmetric beamsplitter and mirror sequence for a range of two-photon Rabi frequencies (assuming $\Omega_R^{+} = \Omega_R^{-}$). The mirror fidelity is defined here as $|e_{+1}|^2$, for an initial state of $|e_{-1}\rangle$ (measuring the population transfer) and the beamsplitter fidelity is defined as $1 - \||e_{+1}|^2 - \frac{1}{2}| - \||e_{-1}|^2 - \frac{1}{2}|$, for an initial state of $|g_0\rangle$
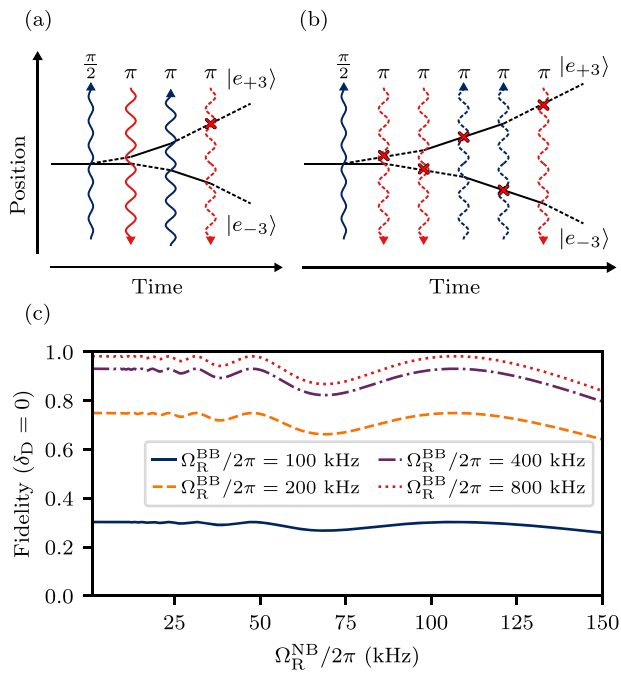
Figure 3. (a) and (b) Show space-time diagrams for two different LMT $N = 3$ state-symmetric beamsplitter sequences. Vertical arrows represent pulses for the two possible Raman transitions ($+$ and $-$); solid (dashed) arrows represent broadband (narrowband) pulses. Red crosses indicate where a particular pulse should not interact with a specific arm. (c) Shows the resonant fidelities of the mirror equivalent of (a), composed of pulses with a rectangular amplitude profile and fixed phase, as the Rabi frequencies of the narrowband and broadband pulses (Ω_R^{NB} and Ω_R^{BB} respectively) are varied.

(measuring how equal the resulting superposition state is). Throughout this paper, we refer to these two quantities as state-transfer fidelities. The resonant state-transfer fidelities of both the mirror and beamsplitter generally decrease with increasing Rabi frequency and hence bandwidth because the individual pulses are less able to distinguish between the two interferometer arms, the only exceptions being when, as shown in figure 2(c), the unwanted arm undergoes an integer number of Rabi cycles.

2.1. Large-momentum-transfer in state-symmetric interferometers

Like non-symmetric Raman pulse atom interferometers, the state-symmetric interferometer design may be extended to enable LMT, where the beamsplitter pulse sequence is designed to create a superposition of states with momenta $\pm N\hbar k_{eff}$, where N is the LMT 'order'. Figure 3 depicts two different ways of creating a large momentum state-symmetric beamsplitter using sequences of Raman pulses. In figure 3(a), the $N = 1$ beamsplitter sequence from figure 2 is extended by two additional high-power (broadband) π pulses in alternating directions. These two pulses should ideally be resonant with—and impart recoil kicks to—both arms simultaneously. Alternatively, in figure 3(b), these two extra broadband pulses are instead split into 4 low-power (narrowband) pulses which are intended to impart kicks to individual arms only.

When using rectangular π pulses, each beamsplitter design has significant drawbacks. For example, in the broadband pulse design in figure 3(a), the fidelity of the extra π pulses drops as the arms separate in momentum and hence resonance frequency. This is shown in figure 3(c), where we have depicted the $N = 3$ resonant mirror pulse sequence fidelity as the Rabi frequencies of the two broadband pulses are varied. We see that high Rabi frequencies and hence laser powers are required to maintain 100% pulse fidelity even on resonance. We also observe that if the broadband Rabi frequency is high enough, the Rabi frequency of the single narrowband pulse may be higher than is possible with the $N = 1$ beamsplitter sequence without incurring fidelity loss. This is because the arms are separated by a larger amount in detuning in the $N = 3$ interferometer.

In comparison, the alternative design employing only narrowband pulses permits 100% efficiency on resonance without requiring prohibitively high Rabi frequencies. However, the velocity acceptance of any order N beamsplitter sequence using this design is limited by that of the first narrowband π pulse in the sequence, which must be sufficiently selective in detuning to avoid exciting the $|e_{+1}\rangle \rightarrow |g_{+2}\rangle$ transition.

3. Indistinguishable momenta and temperature limits

In all atom interferometers, atoms are initially prepared in a single internal state with individual momenta distributed according to the temperature of the atomic cloud. In a general state-symmetric atom interferometer, the beamsplitter diffracts each atom into a superposition of two equal and opposite momenta and the same internal state:

$$|g_0\rangle \rightarrow \frac{1}{\sqrt{2}}\big(|e_{-N}\rangle + |e_{+N}\rangle\big). \quad (4)$$

The mirror, after a period of free evolution, must swap each part of the superposition, providing a $+2N\hbar k_{eff}$ momentum kick to the lower arm $|e_{-N}\rangle$, and a $-2N\hbar k_{eff}$ momentum kick to the upper arm $|e_{+N}\rangle$. This means that the mirror must be able to distinguish both parts of the superposition produced by the beamsplitter and hence that the momentum distribution must be sufficiently narrow to avoid overlap between the two arms [39]. There is therefore an upper limit on the velocity acceptance of any symmetric interferometer, which depends on the size of the separation in momentum produced by the beamsplitter (the momentum order N). This means that by increasing the momentum separation, one can theoretically allow more atoms from a higher temperature source to participate in the interferometer, removing the need for velocity selection using 'blow-away' pulses. This is because symmetric Raman interferometers of the type described in section 2 require a pulse to selectively address one arm of the interferometer, which becomes easier when the momentum difference between the arms is larger.

In figure 4, we have plotted atomic momentum distributions corresponding to two different temperatures following $N = 1$ and $N = 3$ beamsplitter operations to illustrate how larger momentum separations enable the mirror pulse to distinguish
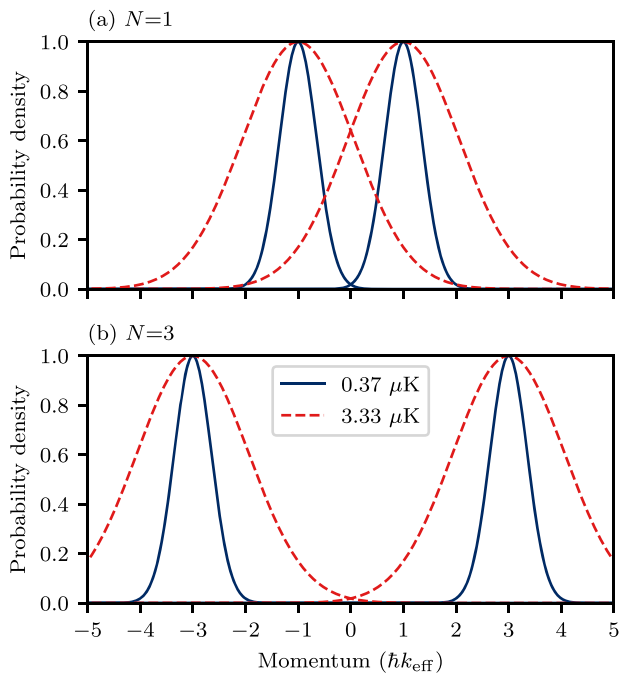
Figure 4. Post-beamsplitter momentum distributions shown following ideal (a) $N = 1$ and (b) $N = 3$ beamsplitters for temperatures of 0.37 μK and 3.33 μK. The large-momentum $N = 3$ beamsplitter places the hotter distribution into a superposition where the two arms are distinguishable, but in the first-order beamsplitter the same temperature results in considerable overlap between the two arms.

between interferometer arms at higher temperatures. We have made the simplification that each beamsplitter produces the desired superposition state irrespective of the initial atomic velocity as we are interested in highlighting the theoretical upper-limit of the process. The momentum distributions for each arm are taken to be Gaussian and are shown for the largest temperatures for which 96% of the atoms have distinguishable velocities in each case.

Even though we have shown that the theoretical limit of the initial momentum width increases for large-momentum symmetric beamsplitters, producing large-momentum superpositions using Raman pulses requires a combination of multiple broadband and/or selective pulses. The broadband pulses must simultaneously transfer momentum to all atoms in each arm as the resonance conditions separate, and the narrowband pulses must transfer all atoms in one arm but not interact with those in another.

4. Optimal control methods

In this section, we explain how we design tailored beamsplitter and mirror pulse sequences with alternating wave-vector directions for any momentum order N symmetric interferometer. These sequences are found by adapting open-loop optimal control theory—specifically the Gradient Ascent Pulse Engineering (GRAPE) algorithm [24]—and are designed to produce high-contrast interferometer fringes for significantly broader initial atomic momentum distributions than is possible

when using sequences of rectangular $\pi/2$ and π pulses. In comparison with rectangular pulses where the laser phase and intensity remain fixed during each interaction, we exploit the fact that it is possible to vary the laser phase and intensity as a function of time in our optimization.

Suppose we have a pulse sequence with a specific order of wave-vector directions, e.g. $+ - + -$, where the relative laser phase ϕ_L and Rabi frequency $\Omega_R^{\pm}$ are piece-wise constant functions of time with a common time-step duration Δt such that the total number of time-steps in the pulse is M. This means each constituent $+$ and $-$ subpulse is specified by a vector of laser phases and Rabi frequencies (amplitudes). During a $+(-)$ subpulse, the controls for the $-(+)$ direction are constrained to be zero to avoid double-diffraction. For a given pulse sequence we therefore have four Cartesian control vectors $\mathbf{c}^j = \{X^+(t_k), Y^+(t_k), X^-(t_k), Y^-(t_k)\}$ where $k = 1, \ldots, M$, $X(t) \equiv \Omega_R \cos \phi_L$, and $Y(t) \equiv \Omega_R \sin \phi_L$. For convenience, we flatten these into a single control vector $\mathbf{c}$ of length $4M$.

The specific order of wave-vector directions in the overall sequence determines the dimension of the state-space and allows us to find an explicit form for the Hamiltonian during a given time-step within a $+$ or $-$ subpulse respectively (shown in appendix A). We can then compute the pulse propagator, representing the time-evolution of the entire sequence,

$$\hat{U}(\mathbf{c}) = \hat{U}_M \hat{U}_{M-1} \ldots \hat{U}_k \ldots \hat{U}_2 \hat{U}_1, \tag{5}$$

where $\hat{U}_k$ is the propagator for the kth time-step.

GRAPE allows us to find waveforms of phase $\phi_L(t)$ and amplitude $\Omega_R^{\pm}(t)$ that maximize fidelities of the general form

$$\mathcal{F}(\mathbf{c}) = f(\langle \psi_T | \hat{U}(\mathbf{c}) | \psi_0 \rangle), \tag{6}$$

where $|\psi_T\rangle$ is the target state, $|\psi_0\rangle$ is the initial state, and f is some differentiable function of the overlap between the final and target states. For example, if f is the modulus-square, then the fidelity represents how well the pulse sequence transfers a given atom from initial to target states. Penalties such as those that enforce smooth solutions or limit the maximum amplitude during a pulse may easily be subtracted from $\mathcal{F}$ [40]. If we require a pulse that maximizes the chosen fidelity under a range of conditions, e.g. for a range of initial momenta, then we can engineer robustness by performing ensemble optimization [31, 41] where the ensemble includes the variations in those conditions.

At its heart, GRAPE is simply an efficient method of computing the local gradient of $\mathcal{F}$ with respect to each phase and amplitude value in the entire control vector. Once the gradient is computed, one can ascend the fidelity landscape towards a peak: an optimized pulse of high fidelity. Second derivatives of the fidelity with respect to the controls provide curvature information which enables enhanced convergence through Newton-type methods [42, 43]. Computing second derivatives is generally computationally expensive, so quasi-Newton approaches—which approximate them through a history of gradients—are generally preferred. One popular example is the limited-memory Broyden–Fletcher–Goldfarb–Shanno (L-BFGS) method [44], which we use for the optimization in this work.

J. Phys. B: At. Mol. Opt. Phys. **55** (2022) 205501

J Saywell *et al*

4.1. Measures of performance and velocity-acceptance

In order to optimize the pulses in our interferometer, we must first specify the correct fidelities for the beamsplitters, mirrors, and recombiners. Our order-N beamsplitter pulse sequence, represented by the pulse propagator $\hat{U}_{\mathrm{bs}}$ must transfer atoms initially in the state $|g_0\rangle$ to an equal superposition of $|e_{-N}\rangle$ and $|e_{+N}\rangle$ for odd N ($|g_{-N}\rangle$ and $|g_{+N}\rangle$ for even N). We therefore define the following individual-atom fidelity

$$\mathcal{F}_{\mathrm{bs}}^N(\mathbf{c}, v) = |\langle\psi_{\mathrm{T}}(v)|\hat{U}_{\mathrm{bs}}(\mathbf{c}, v)|g_0\rangle|^2, \qquad (7)$$

where the target state (for odd N) is given by

$$|\psi_{\mathrm{T}}(v)\rangle = \frac{1}{\sqrt{2}}(|e_{-N}\rangle + e^{i\phi(v)}|e_{+N}\rangle), \qquad (8)$$

where ϕ is the target superposition phase. In order to obtain high fidelities in the optimization, we have found it necessary to define the target phase to be a linear function of the initial atomic velocity, such that $\phi(v) = 2Nk_{\mathrm{eff}}v\tau$, where τ is the total pulse duration. This way, after the pulse, a given atom ends up in a superposition whose phase is equivalent to that which would have accrued in a period of free evolution equal to the pulse duration.

Our mirror pulse sequences must swap the two arms of the interferometer, performing the operation

$$\frac{1}{\sqrt{2}}(e^{i\phi}|e_{-N}\rangle + |e_{+N}\rangle) \rightarrow \frac{1}{\sqrt{2}}(|e_{-N}\rangle + e^{i\phi}|e_{+N}\rangle), \quad (9)$$

for all possible input superposition phases ϕ. It is vital that the phase of the input superposition state is not modified in a different way for different atoms, because to do so would scramble any interferometric measurement. We therefore simultaneously optimize a series of state-to-state fidelities and average them

$$\mathcal{F}_m^N(\mathbf{c}, v) = \frac{1}{N_\phi}\sum_{i=1}^{N_\phi} |\langle\psi_{\mathrm{T}}(\phi_i)|\hat{U}_m(\mathbf{c}, v)|\psi_{\mathrm{i}}(\phi_i)\rangle|^2, \qquad (10)$$

where the initial and target states ($|\psi_{\mathrm{i}}(\phi)\rangle$ and $|\psi_{\mathrm{T}}(\phi)\rangle$) are those appearing in equation (9) and the individual fidelities are averaged over a range of N_ϕ input superposition phases between $-\pi$ and π.

The recombiner pulse sequence may be obtained from the beamsplitter sequence by using the 'flip-reverse' construction procedure [33, 45], where the beamsplitter phase and amplitude profiles are time-reversed and the phase profile is inverted ($\phi_{\mathrm{L}}(t) \rightarrow -\phi_{\mathrm{L}}(\tau - t)$). This also involves reversing the order of wave-vector directions. This 'flip-reverse' procedure produces a pulse that cancels the velocity-dependent phase introduced by the beamsplitter and correctly converts any relative phase accumulated between the $\pm N\hbar k_{\mathrm{eff}}$ states into a population difference between the states $|g_0\rangle$ and $|e_{+1}\rangle$.

Since our aim is to find pulses that improve the velocity acceptance of the interferometer, for each pulse we maximize an ensemble fidelity $\Phi_{\mathrm{bs,m}}$ where the ensemble is defined by a symmetric range of N_v input velocities (Doppler shifts) $\{-v_{\mathrm{max}}, \ldots, v_{\mathrm{max}}\}$ and hence engineer robustness to variations

in the initial atomic momenta. The larger the range of input momenta included in this ensemble, the larger the velocity acceptance of the optimized pulse.

It is also important that while reducing the sensitivity of the pulses to variations in the initial atomic velocity we do not make the pulse sequences more sensitive to variations in laser intensity (which manifest as variations in the two-photon Rabi frequency). We therefore also average our fidelities over a range of N_ε amplitude errors $\{\varepsilon_{\mathrm{min}}, \ldots, \varepsilon_{\mathrm{max}}\}$ (assumed constant for the duration of individual sequences). We define an amplitude error as $\varepsilon \equiv \Omega_{\mathrm{R}}^{\mathrm{max}}/\Omega_{\mathrm{eff}}$ where $\Omega_{\mathrm{R}}^{\mathrm{max}}$ is the actual maximum Rabi frequency and Ω_{eff} is the intended maximum Rabi frequency during the pulse [46].

We therefore arrive at the following ensemble fidelities for our beamsplitter and mirror pulses:

$$\Phi_{\mathrm{bs,m}}(\mathbf{c}) = \frac{1}{N_v N_\varepsilon} \sum_{v=-v_{\mathrm{max}}}^{v_{\mathrm{max}}} \sum_{\varepsilon=\varepsilon_{\mathrm{min}}}^{\varepsilon_{\mathrm{max}}} \mathcal{F}_{\mathrm{bs,m}}^N(\mathbf{c}, v, \varepsilon). \qquad (11)$$

We subtract two weighted penalty terms [40] from our ensemble-averaged fidelity: a derivative-norm-square (DNS) penalty to constrain waveform smoothness, and a spillout-norm-square (SNS) penalty to constrain the maximum Rabi frequency to Ω_{eff}. These penalty terms may be written as:

$$\mathcal{P}_{\mathrm{DNS}}(\mathbf{c}^j) = \frac{1}{M}\sum_{k=1}^{M}\left(\sum_{l=1}^{M}\hat{D}_{kl}c_l^j\right)^2, \qquad (12)$$

$$\mathcal{P}_{\mathrm{SNS}}(\mathbf{c}) = \begin{cases} \dfrac{1}{2M}\displaystyle\sum_{k=1}^{4M}(|c_k| - A)^2, & |c_k| > A \\ 0, & |c_k| \leqslant A \end{cases} \qquad (13)$$

$\hat{D}$ is a finite-difference operator which computes the second-order derivative of a control vector with respect to time and $A \equiv \Omega_{\mathrm{eff}}/\sqrt{2}$.

5. Results

We have optimized three separate symmetric interferometer sequences corresponding to momentum orders of $N = 1, 2$, and 3. For each momentum order, we constructed our optimized pulses from the smallest number of subpulses with alternating wave-vector directions necessary to reach the target states. For example, the $N = 3$ beamsplitter sequence was $+ - + -$ and the corresponding mirror sequence was $+ - + - + - +$. Furthermore, we restricted the duration of each $+$ and $-$ subpulse to be identical and optimized our pulses with no time delay between the wave-vector switching [47].

For each momentum order, we have optimized our pulses to be robust to different ranges of input momenta such that the desired velocity-acceptance increases with N. $v_{\mathrm{max}} = 0.5, 1$ and 1.5 (units of $\hbar k_{\mathrm{eff}}/m$) for $N = 1, 2$, and 3 respectively. $\varepsilon_{\mathrm{min}} = 0.95$ and $\varepsilon_{\mathrm{max}} = 1.05$ for all optimizations carried out in this work.

We have optimized our pulses allowing the Rabi frequency and relative laser phase to vary with time, subject to penalties
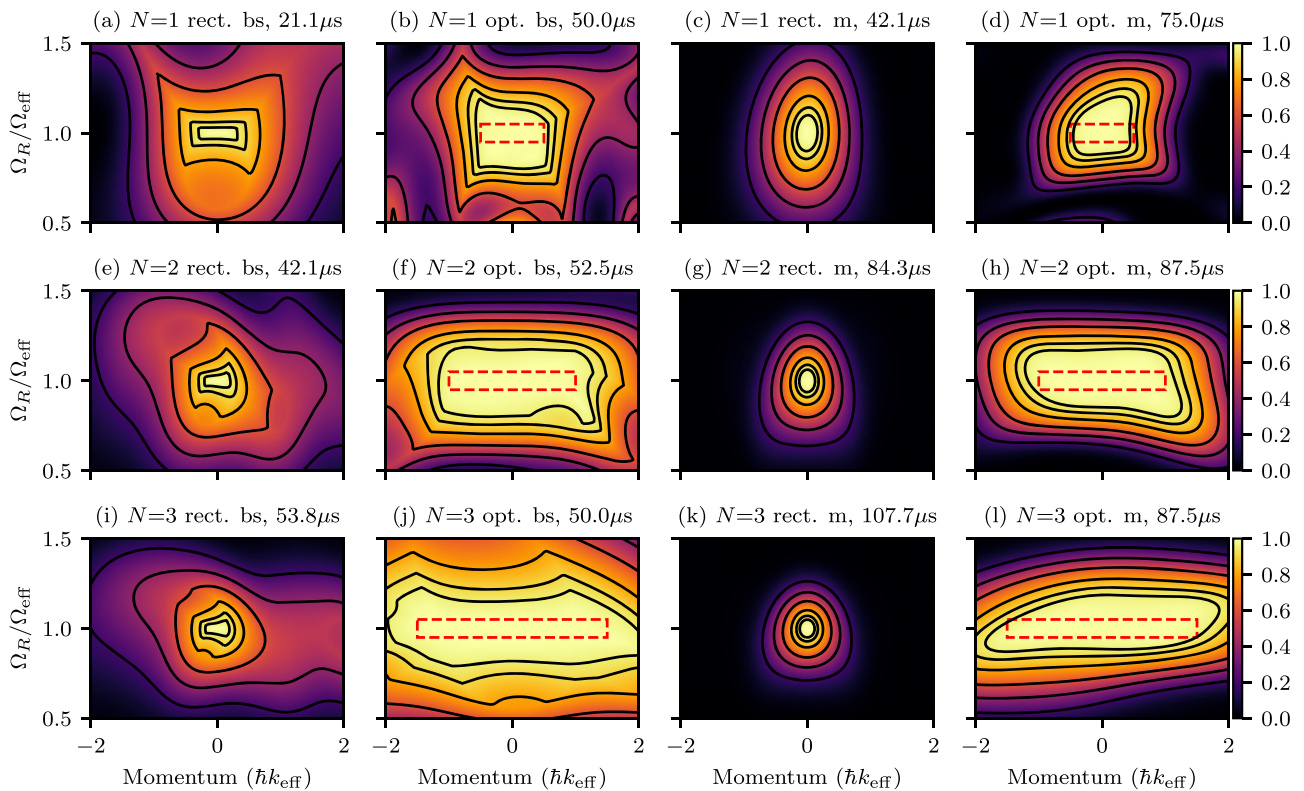
J. Phys. B: At. Mol. Opt. Phys. **55** (2022) 205501

J Saywell *et al*

Figure 5. Simulated state-transfer fidelities of rectangular ((a), (c), (e), (g), (i) and (k)) and optimized ((b), (d), (f), (h), (j) and (l)) symmetric Raman pulses for momentum orders of $N = 1$, 2, and 3 shown as a function of initial atomic momentum on the *x*-axis and the amplitude error on the *y*-axis. Beamsplitter (bs) pulses are shown in the first two columns; mirror (m) pulses are shown in the final two. For the optimized pulses the region of optimization is indicated by the red dashed box. The contours are at 0.2, 0.4, 0.6, 0.8, 0.9, and 0.95. Axis labels include the total duration of each composite pulse sequence showing that, as N is increased, optimized sequences can be significantly shorter than their rectangular counterparts.

on the waveform smoothness and maximum Rabi frequency (applied above an experimentally feasible limit of 200 kHz). Furthermore, we restricted the Rabi frequency at the beginning and end of each pulse sequence to be zero, to prevent spikes in amplitude appearing at the beginning and end of the sequences. The pulses were optimized using the L-BFGS GRAPE algorithm implemented in the nuclear magnetic resonance (NMR) Spinach spin dynamics toolbox [48]. The initial guess for the waveforms was a random phase and amplitude profile, and the algorithm was set to terminate either following 1000 iterations or if the norm of the gradient fell below 10^{-6}. The update step size used in a given iteration of the L-BFGS optimization is calculated using the cubic line search algorithm detailed in [40]. Due to the nature of numerical optimization, there is no guarantee we have found the best pulses for the chosen parameters, and more exploration of the fidelity landscape may be required to do this.

5.1. Optimized state-symmetric pulse sequences

Figure 5 shows the simulated state-transfer efficiency of rectangular and optimized pulse sequences for symmetric beamsplitter and mirror pulses, respectively. The fidelities are shown as a function of initial atomic momentum and amplitude error. The red dashed boxes correspond to the target velocity acceptance and amplitude error robustness of the optimized pulses.

The rectangular pulse sequences were composed entirely of narrowband π and $\pi/2$ pulses (the design shown in figure 3(b)) with Rabi frequencies chosen such that the unwanted transitions for each π pulse in the sequence occur at the first zero in the π pulse sinc-squared spectrum. We observe a significant increase in the velocity acceptance with the optimized pulses and, further, that this increases as the momentum order is increased. In comparison, the velocity acceptance of the rectangular pulse sequences is limited for all N by that of the $N = 1$ sequence.

Figure 5 also indicates the total duration of each pulse sequence; we observe that the duration of the optimized sequences does not increase significantly with momentum order—indeed the durations of the $N = 1$ and $N = 3$ beamsplitters are identical. This is because it becomes easier to optimize symmetric beamsplitter and mirror sequences as N is increased.

The amplitude and phase profiles for the optimized pulses simulated in the contour plots are displayed in figure 6 along with their ensemble fidelities (equation (11)). It is hard to discern a clear pattern to the results of the optimization, but we notice that sometimes the mirror pulse is optimized with a time-symmetric amplitude profile and a time anti-symmetric phase profile and that these properties preserve the superposition phase in the transformation of equation (9). The sudden 2π jumps apparent in the phase profiles are artefacts of the
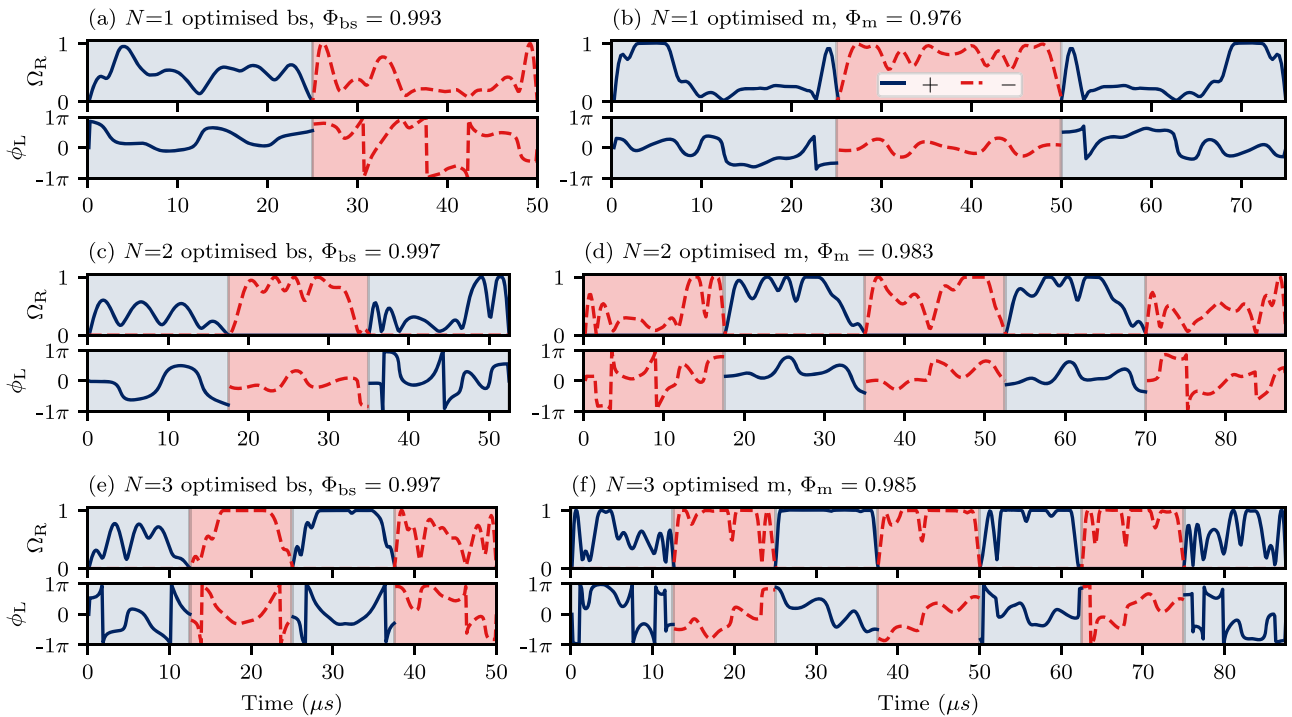
Figure 6. Optimized phase and amplitude profiles corresponding to optimized symmetric beamsplitter and mirror sequences for interferometers of order $N = 1$ to $N = 3$. In these plots, we have factored the maximum Rabi frequency Ω_{eff} out of the pulse amplitudes. The terminal ensemble fidelities reached by the optimization are shown above each panel. Positive and negative wave-vector directions (subpulses) are represented by blue (solid) and red (dashed) waveforms respectively and only one wave-vector has a non-zero Rabi frequency at any one time, alternating between pre-defined (shaded) periods. Each subpulse consists of 100 time-steps, except the pulse in (a) which has 200 steps per subpulse.

graphical representation: the Cartesian waveforms $\Omega_{\text{R}} \cos \phi_{\text{L}}$ and $\Omega_{\text{R}} \sin \phi_{\text{L}}$ are smooth functions of time.

As an illustration of how the optimized symmetric pulses work, we have simulated the state probabilities throughout the $N = 2$ beamsplitter sequence for a resonant atom in figure 7. We observe that each subpulse within the optimized sequence performs the same role identified in the schematic of figure 3(a): starting in the state $|g_0\rangle$, the first subpulse creates a superposition of $|g_0\rangle$ and $|e_{+1}\rangle$; the second subpulse (in the opposite direction) transfers $|g_0\rangle$ to $|e_{-1}\rangle$ and $|e_{+1}\rangle$ to $|g_{+2}\rangle$; the final subpulse then transfers $|e_{-1}\rangle$ to $|g_{-2}\rangle$ leaving the other arm (state $|g_{+2}\rangle$) untouched. The first subpulse takes the role of the $\pi/2$ pulse, the second acts as a broadband π pulse, and the final as a narrowband π pulse.

5.2. Interferometer contrast

In this section, we explain how we simulate the expected interferometer fringe contrast following a state-symmetric order N interferometer at a given cloud temperature, and compare the results for the optimized and rectangular pulse sequences.

Starting with an atom with non-zero momentum p in the z-direction, we compute the final state following the beamsplitter pulse sequence and remove all residual population in unwanted states, preserving the two primary interferometer arms for the chosen momentum order N, e.g. $|e_{+N}\rangle$ and $|e_{-N}\rangle$. This state-purification is roughly equivalent to performing a blow-away operation except all unwanted momentum orders are removed not just those in a particular electronic state. Following a

period of free evolution, we evolve the state of both arms under the mirror pulse sequence and repeat the state-purification step. We then apply a second period of free evolution (of equivalent duration to the first to cancel the momentum-dependent acquired phase), and introduce a relative phase ϕ_{int} between the two arms. Finally, we apply the combined propagator for the recombiner pulse sequence ($\hat{U}_{\text{re}}$, also a function of p) and compute the probability of finding the atom in the state $|e_{+1}\rangle$. This probability—a function of initial atomic momentum—is given by

$$P_e(p) = \left| \langle e_{+1} | \hat{U}_{\text{re}} \left(|\psi_{\text{u}}(p)\rangle + e^{i\phi_{\text{int}}} |\psi_{\text{d}}(p)\rangle \right) \right|^2, \quad (14)$$

where $|\psi_{\text{d}}\rangle(p)$ and $|\psi_{\text{u}}\rangle(p)$ are the states prior to the final pulse in the lower and upper interferometer arms, respectively.

We then perform numerical integration of equation (14) over a Gaussian distribution of initial atomic momenta corresponding to a specific temperature and fit a sinusoid to the resulting thermally-averaged probability for a range of relative phases ϕ_{int}. The amplitude of the fitted sinusoid is interpreted as the thermally-averaged interferometer contrast following a particular interferometer sequence.

The results of the contrast simulation are shown in figure 8 for rectangular and optimized sequences. We observe that the optimized pulses increase the contrast at all simulated cloud temperatures and, further, that the higher the momentum separation (N), the higher the contrast for a given cloud temperature. For example, the $N = 3$ optimized sequence yields

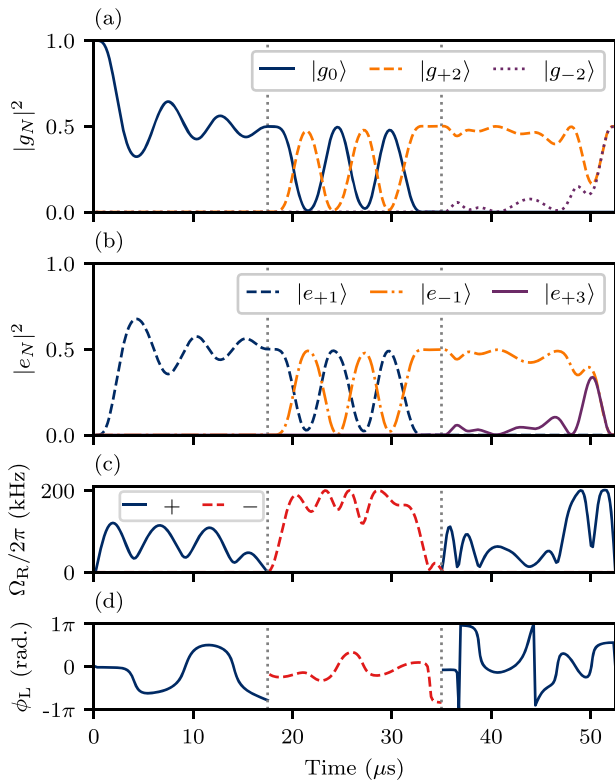J. Phys. B: At. Mol. Opt. Phys. **55** (2022) 205501

J Saywell *et al*

Figure 7. State probabilities for $|g_n\rangle$ (a) and $|e_n\rangle$ (b) states computed during the $N = 2$ beamsplitter pulse as a function of time. The amplitude and phase waveforms from figure 6(c) are reproduced on axes (c) and (d) for reference. The atom is initially at rest in the state $|g_0\rangle$. By the end of the sequence, it is in an equal superposition of $|g_{-2}\rangle$ and $|g_{+2}\rangle$.

Figure 8. Simulated contrast for interferometers of orders $N = 1, 2, 3$ using rectangular pulses (a) and GRAPE-optimized pulses (b). The rectangular pulse sequences consist of entirely narrowband pulses.

greater than 95% contrast at a temperature of 1 μK where the $N = 3$ rectangular sequence results in a contrast below 20%.

5.3. 'Blow-away' compatible optimized pulses

A key feature of the state-symmetric interferometer scheme introduced by Berg *et al* in [22] was that it allowed a state-purification or 'blow-away' pulse to be applied *after* the initial beamsplitter. This pulse is designed to remove atoms in a particular internal state e.g. $|g\rangle$ or $|e\rangle$, and since the beamsplitter produces a superposition of atoms in the same internal state $|e\rangle$, can be applied after the beamsplitter pulse. This removes the need for a long velocity-selective π pulse before the beamsplitter (as is often used in conventional Raman interferometers). The symmetric beamsplitter in [22] therefore provides an automatic velocity selection of the atomic sample.

Although we have demonstrated that optimal control can significantly increase the velocity acceptance of the interferometer pulses as the momentum order of the diffraction is increased, if we inspect the final state probabilities following the optimized beamsplitters for a range of input momenta (figure 9(a)), we see that they are not compatible with blow-away pulses: there is significant population in the excited state following the pulses for large input momenta.

However, we can modify our beamsplitter fidelity to ensure that outside the central detuning pass-band (the detuning range
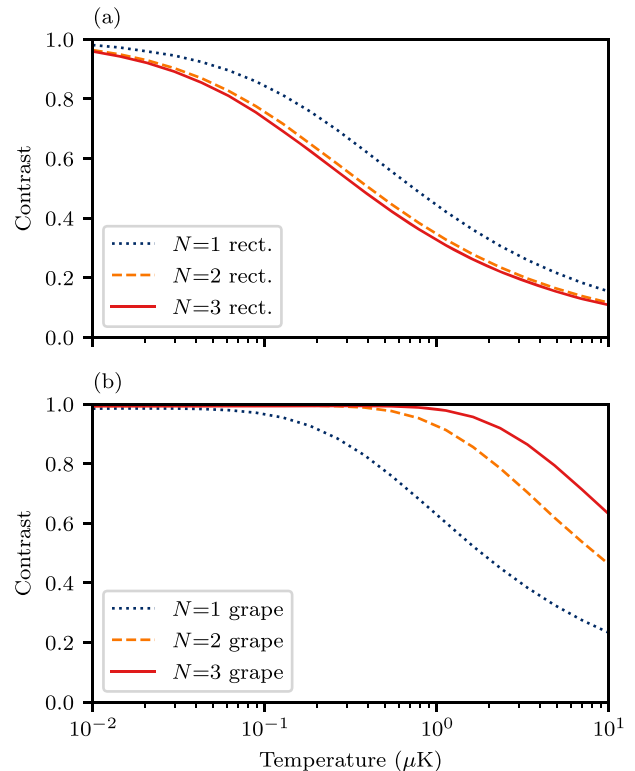
in which we desire an equal superposition of target states), there is a stop-band (sb) where all the population is directed into the ground state, therefore enabling blow-away pulses after the beamsplitter. For the $N = 1$ beamsplitter sequence, this modification amounts to minimising the population in the 'loss' states $|e_{-1}\rangle$ and $|e_{+1}\rangle$ in the sb, since the only possible excited states that are reachable after the $+-$ sequence are $|e_{-1}\rangle$ and $|e_{+1}\rangle$. In the optimisation, this is done by subtracting the following loss term from the ensemble fidelity defined in equation (11):

$$\mathcal{P}_{\text{loss}}(\mathbf{c}) = \frac{1}{N_v^{\text{sb}}} \sum_{v \in \text{sb}} \sum_{\text{loss}} |\langle \psi_{\text{loss}} | \hat{U}_{\text{bs}}(\mathbf{c}, v) | g_0 \rangle|^2. \quad (15)$$

N_v^{sb} represents the number of atomic momenta in the sb. For the $N = 3$ case, where the number of allowed states is larger, this amounts to simultaneously minimising the population in the loss states $|\psi_{\text{loss}}\rangle$: $|e_{-1}\rangle$, $|e_{+1}\rangle$, $|e_{-3}\rangle$, and $|e_{+3}\rangle$ in the sb. Minimising these quantities forces atoms to diffract into the higher momentum order $|g\rangle$ states or remain in the initial state outside the pass-band therefore enabling state purification after the pulse.

The results for this selective optimization for a momentum order of $N = 3$ are shown in figure 9 and compared with the equivalent $N = 3$ beamsplitter from figure 6. We do not consider such a modification to the order $N = 2$ beamsplitter sequence, as it produces a superposition of atoms in the internal state $|g\rangle$ from atoms initially in the internal state $|g\rangle$
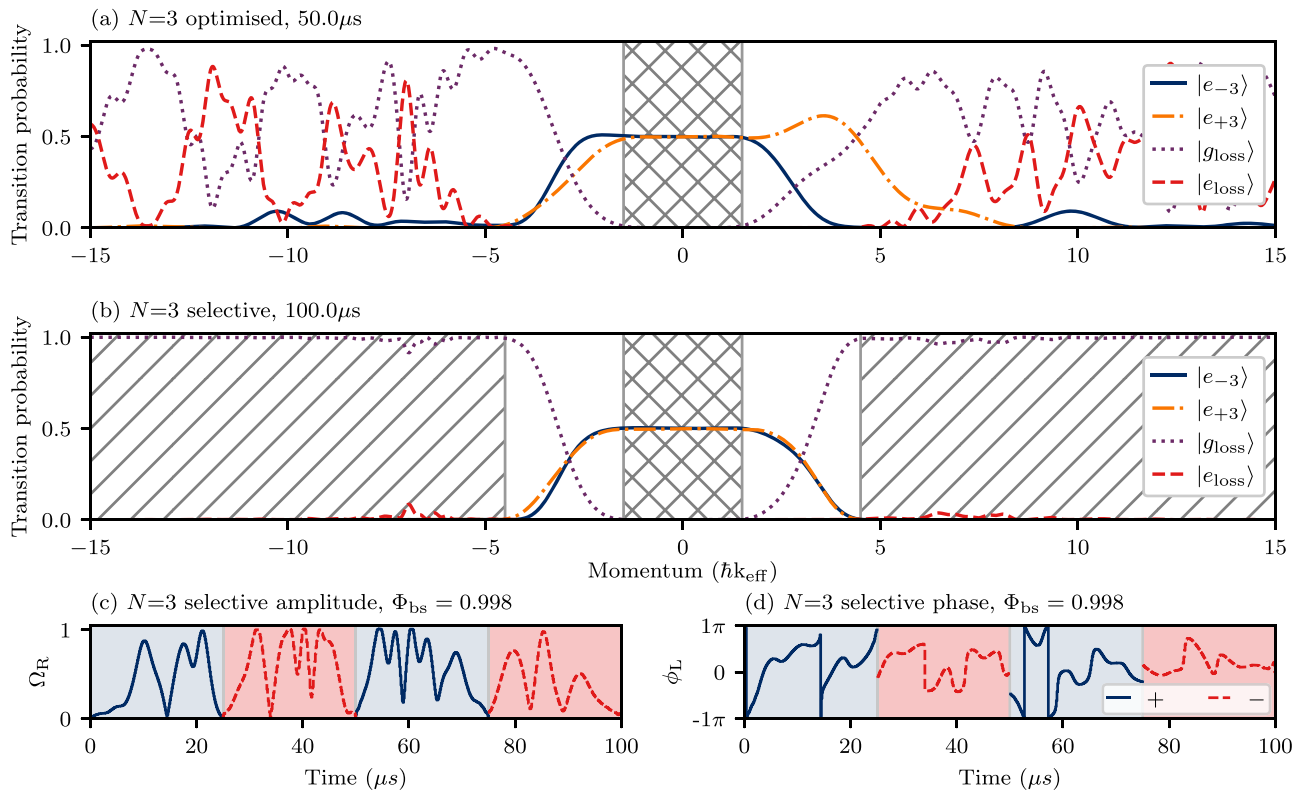
Figure 9. (a) and (b) Show the transition probability for different states following two optimized $N = 3$ beamsplitter pulse sequences as a function of atomic momentum. Both beamsplitters are optimized to produce an equal superposition of $|e_{-3}\rangle$ and $|e_{+3}\rangle$ in the central (cross-hatched) region. The total loss to unwanted momentum states is represented, divided by electronic state, as $|g_{\text{loss}}\rangle$ and $|e_{\text{loss}}\rangle$. This loss becomes significant for large input momenta but, while in (a) it is distributed across both hyperfine levels, in (b) it is largely restricted to $|g_n\rangle$ by explicitly minimising excitation to $|e_n\rangle$ states in the hatched stop band. This allows atoms in unwanted states to be removed with a 'blow-away' pulse, at the expense of increased pulse duration. (c) and (d) Show the amplitude and phase profiles, respectively, for this blow-away compatible (selective) pulse. Each subpulse consists of 200 time-steps and the total sequence duration is 100 μs, which is twice that of the $N = 3$ beamsplitter presented in figure 6. The amplitude profile shown in (c) also possesses significantly smoother rises and falls.

and therefore the limiting behaviour at large detuning is not compatible with a removal of atoms in the wrong state. We have found that these blow-away compatible pulses needed to be longer to reach similar fidelities to the ones in section 5, and observe that there is still some small loss to the excited state within the sb.

6. Discussion

State-symmetric Raman interferometers—like those employing Bragg pulses—minimize the effect of laser phase noise and magnetic noise during the dwell-times but require sub-recoil cloud temperatures for high diffraction efficiency. Velocity selection is therefore necessary, inevitably discarding atoms that move too quickly and thus lowering the measurement SNR. In this paper, we have shown how Raman pulse sequences designed using optimal control can increase the velocity acceptance of this type of interferometer, enabling one to potentially forgo the velocity selection step and hence use more atoms in inertial measurements.

In addition, we have explained how increasing the momentum imparted by the diffraction process allows one to further lift the constraints on the initial temperature of the atoms. This is because (a) larger momentum superpositions are easier to

distinguish with frequency selective pulses that affect only one interferometer arm at a time and (b) optimized pulses can create these larger momentum superpositions with high fidelity. In all these applications, the rectangular π pulse is limited by its sinc-squared excitation profile; optimized pulses can be designed with tailored frequency selectivity and robustness enabling higher fidelity sequences to be obtained.

A key argument in this paper is that optimal control can remove the need for velocity selection in state-symmetric Raman-based interferometers. Velocity selection often involves using a long, low-power π pulse to select a sub-recoil distribution from a $\sim \mu K$ atom cloud. However, the atomic sample also typically needs to be prepared in a single Zeeman substate in interferometers designed to detect inertial effects. Although Zeeman state preparation can be performed concurrently with velocity selection by using a bias magnetic field to separate the substates in frequency before applying the selective π pulse, it can also be performed without velocity selection using optical pumping [49] and/or microwave pulses [6]. It therefore remains useful to develop techniques that enable high-contrast interferometry without velocity selection.

In the pulses optimized in this paper, the laser intensity varies in time. This means the AC Stark shift (present in the Raman resonance condition of equation (1)), changes during

the pulses. Since this effect was not included in our model, it must be compensated experimentally. This can be done by adjusting the intensity ratio of the two Raman beams [37] or by using additional off-resonant frequency components in the Raman beams [50]. Alternatively, the AC Stark shift could be included in the optimization itself, or the optimization could be restricted to phase-varying pulse sequences only.

Spontaneous emission from unwanted single-photon excitation will limit any practical improvement in fringe contrast and pulse area that may be obtained using optimized pulse sequences because they are longer than those composed of rectangular pulses. The rate of spontaneous emission can be reduced in Raman transitions by increasing the single-photon detuning from the upper intermediate levels (at a cost of reduced Rabi frequency if the laser intensity is not also increased) although this can prevent one compensating the AC Stark shift using the intensity ratio technique. In practice therefore, it is vital that spontaneous emission is minimized as much as possible and that one uses the shortest possible optimized sequences.

We have optimized our interferometer pulses assuming that the Rabi frequency and the Doppler detuning do not change significantly in time. If there is an intensity imbalance between pulse sequences (i.e. between beamsplitter, mirror, and recombiner) resulting from, for example, expansion of the atomic cloud within a beam with a spatial intensity gradient, the phase spread introduced by first pulse sequence will thus not perfectly cancel with the final one. This leads to a phase shift in the interferometer fringe (analogous to the effect explored first by Gillot *et al* [51]). This could be reduced by limiting the intensity variation experienced by the expanding atom cloud by using bigger beams, or by directly compensating for this effect in the optimization. Note that this effect is minimized when maximizing the beamsplitter fidelity over a range of different amplitude errors, meaning the same linear phase spread should be applied and later reversed despite variations in intensity—but it is not perfect unless the fidelity is 100%.

Finally, we note that the framework presented in this paper can be extended to optimize pulses for Raman double-diffraction schemes (as outlined in appendix A) and other interferometer designs that employ multi-pulse sequences, such as the algorithmic cooling scheme introduced by Freegarde and Segal [52] as it utilizes the ladder of momentum states addressed by sequences of laser pulses in alternating directions.

Data availability statement

The data that support the findings of this study are available upon reasonable request from the authors.

Appendix A. State-symmetric Raman pulse theory

We write the state of the atom following a general sequence of pulses $+ - + - + - \ldots$ as

$$|\psi\rangle = (g_{-n_{\max}}, \ldots, e_{-1}, g_0, e_1, \ldots, g_{n_{\max}})^{\mathrm{T}}, \quad \text{(A1)}$$

where $n_{\max}$ depends on the specific sequence of effective wave-vector directions.

Following adiabatic elimination of the intermediate state $|i\rangle$ from the dynamics, we can find the equations for the rates of change of the amplitudes $g_n(t)$ and $e_n(t)$ corresponding to the states $|g_n\rangle$ and $|e_n\rangle$, respectively [17,53]. For the $+\hbar k_{\mathrm{eff}}$ transition, we find

$$i\dot{g}_n = \frac{\Omega_{\mathrm{R}}^+}{2} e^{-i\phi_{\mathrm{L}}} e^{i(\delta_{\mathrm{L}} - \delta_{\mathrm{D}} - (1+2n)\delta_{\mathrm{R}})t} e_{n+1} \quad \text{(A2)}$$

$$i\dot{e}_{n+1} = \frac{\Omega_{\mathrm{R}}^+}{2} e^{i\phi_{\mathrm{L}}} e^{-i(\delta_{\mathrm{L}} - \delta_{\mathrm{D}} - (1+2n)\delta_{\mathrm{R}})t} g_n, \quad \text{(A3)}$$

and for the $-\hbar k_{\mathrm{eff}}$ transition, we find

$$i\dot{g}_n = \frac{\Omega_{\mathrm{R}}^-}{2} e^{-i\phi_{\mathrm{L}}} e^{i(\delta_{\mathrm{L}} + \delta_{\mathrm{D}} - (1-2n)\delta_{\mathrm{R}})t} e_{n-1} \quad \text{(A4)}$$

$$i\dot{e}_{n-1} = \frac{\Omega_{\mathrm{R}}^-}{2} e^{i\phi_{\mathrm{L}}} e^{-i(\delta_{\mathrm{L}} + \delta_{\mathrm{D}} - (1-2n)\delta_{\mathrm{R}})t} g_n. \quad \text{(A5)}$$

We have defined Ω_{R}^- and Ω_{R}^+ as the two-photon Rabi frequencies (assumed equal throughout this paper) for the $-$ and $+$ Raman transitions, respectively. $\phi_{\mathrm{L}} \equiv \phi_1 - \phi_2$ is the difference between the phase of each laser beam.

By making the transformation

$$g_n \equiv e^{in(\delta_{\mathrm{D}} + n\delta_{\mathrm{R}})t} \tilde{g}_n \quad \text{(A6)}$$

$$e_n \equiv e^{in(\delta_{\mathrm{D}} + n\delta_{\mathrm{R}})t - i\delta_{\mathrm{L}}t} \tilde{e}_n, \quad \text{(A7)}$$

we can move to a rotating frame and find that for the $+\hbar k_{\mathrm{eff}}$ transition

$$i\dot{\tilde{g}}_n = n(\delta_{\mathrm{D}} + n\delta_{\mathrm{R}})\tilde{g}_n + \frac{\Omega_{\mathrm{R}}^+}{2} e^{-i\phi_{\mathrm{L}}} \tilde{e}_{n+1} \quad \text{(A8)}$$

$$i\dot{\tilde{e}}_{n+1} = [(n+1)(\delta_{\mathrm{D}} + (n+1)\delta_{\mathrm{R}}) - \delta_{\mathrm{L}}]\tilde{e}_{n+1} + \frac{\Omega_{\mathrm{R}}^+}{2} e^{i\phi_{\mathrm{L}}} \tilde{g}_n, \quad \text{(A9)}$$

and for the $-\hbar k_{\mathrm{eff}}$ transition that

$$i\dot{\tilde{g}}_n = n(\delta_{\mathrm{D}} + n\delta_{\mathrm{R}})\tilde{g}_n + \frac{\Omega_{\mathrm{R}}^-}{2} e^{-i\phi_{\mathrm{L}}} \tilde{e}_{n-1} \quad \text{(A10)}$$

$$i\dot{\tilde{e}}_{n-1} = [(n-1)(\delta_{\mathrm{D}} + (n-1)\delta_{\mathrm{R}}) - \delta_{\mathrm{L}}]\tilde{e}_{n-1} + \frac{\Omega_{\mathrm{R}}^-}{2} e^{i\phi_{\mathrm{L}}} \tilde{g}_n. \quad \text{(A11)}$$

We can therefore write the total Hamiltonian for the $+$ direction as $\hat{H} = \hat{H}_0 + \hat{H}_+$, and for the $-$ direction as $\hat{H} = \hat{H}_0 + \hat{H}_-$, noticing that the drift term $\hat{H}_0$ (containing the detuning) is common to each wave-vector direction. As an illustration,

J. Phys. B: At. Mol. Opt. Phys. **55** (2022) 205501

J Saywell *et al*

we depict each matrix in the basis of equation (A1) for the case where $n_{max} = 2$:

$$\hat{H}_0 = \hbar \begin{pmatrix} -2\delta_D + 4\delta_R & 0 & 0 & 0 & 0 \\ 0 & -\delta_D + \delta_R - \delta_L & 0 & 0 & 0 \\ 0 & 0 & 0 & 0 & 0 \\ 0 & 0 & 0 & +\delta_D + \delta_R - \delta_L & 0 \\ 0 & 0 & 0 & 0 & +2\delta_D + 4\delta_R \end{pmatrix}, \quad (A12)$$

$$\hat{H}_- = \frac{\hbar}{2} \begin{pmatrix} 0 & 0 & 0 & 0 & 0 \\ 0 & 0 & \Omega_R^- e^{i\phi_L} & 0 & 0 \\ 0 & \Omega_R^- e^{-i\phi_L} & 0 & 0 & 0 \\ 0 & 0 & 0 & 0 & \Omega_R^- e^{+i\phi_L} \\ 0 & 0 & 0 & \Omega_R^- e^{-i\phi_L} & 0 \end{pmatrix}, \quad (A13)$$

$$\hat{H}_+ = \frac{\hbar}{2} \begin{pmatrix} 0 & \Omega_R^+ e^{-i\phi_L} & 0 & 0 & 0 \\ \Omega_R^+ e^{i\phi_L} & 0 & 0 & 0 & 0 \\ 0 & 0 & 0 & \Omega_R^+ e^{-i\phi_L} & 0 \\ 0 & 0 & \Omega_R^+ e^{+i\phi_L} & 0 & 0 \\ 0 & 0 & 0 & 0 & 0 \end{pmatrix}. \quad (A14)$$

The form of these Hamiltonians makes it clear that, unlike in Raman double diffraction, only adjacent pairs of states are coupled by a pulse in a given direction: the system of equations governing the dynamics is closed. This makes it easier to simulate because there is no need to truncate the ladder of momentum states included in the dynamics. In order to optimise pulses for a double diffraction arrangement, one can write the total Hamiltonian as the sum $\hat{H} = \hat{H}_0 + \hat{H}_+ + \hat{H}_-$, treating the Rabi frequency and relative phase for $+$ and $-$ transitions as the same, and truncate the state-space appropriately.

Once we specify the sequence of wave-vector directions $(+ - + - + - \cdots)$ and hence constrain the dimension of the state-space as explained above, we can write down an expression for the Hamiltonian and exponentiate it to find the propagator for time-evolution under a time-slice of duration Δt with constant Rabi frequency and relative laser phase. Using

$$|\psi(\Delta t + t_0)\rangle = \exp\left(-\frac{i}{\hbar}\hat{H}\Delta t\right)|\psi(t_0)\rangle \quad (A15)$$

we can then simulate the evolution of a particular atom's state under either a $+$ or $-$ pulse of constant Rabi frequency, detuning, and laser phase. Periods of free evolution may also be simulated in this manner, by simply setting $\hat{H} = \hat{H}_0$ in the state propagation.

Examining the drift Hamiltonian in equation (A12), we can also see why state-symmetric interferometers are insensitive to perturbations that affect the laser and hyperfine transition frequencies during the dwell times. Assuming an order N beamsplitter sequence produces a superposition of $|e_{-N}\rangle$ and $|e_{+N}\rangle$ with perfect fidelity, the relative phase that subsequently accrues between each arm when the light is off will depend only upon the difference in the Doppler shift $2N\delta_D$ between these two states. Any change in $\delta_L = \omega_1 - \omega_2 - \omega_{eg}$ will leave this relative phase unaffected.

ORCID iDs

Jack Saywell ⬤ https://orcid.org/0000-0002-7867-2128
Max Carey ⬤ https://orcid.org/0000-0001-5283-5972
Ilya Kuprov ⬤ https://orcid.org/0000-0003-0430-2682
Tim Freegarde ⬤ https://orcid.org/0000-0002-0680-1330

References

[1] Berman P (ed) 1997 *Atom Interferometry* (New York: Academic)
[2] Bongs K, Holynski M, Vovrosh J, Bouyer P, Condon G, Rasel E, Schubert C, Schleich W P and Roura A 2019 Taking atom interferometric quantum sensors from the laboratory to real-world applications *Nat. Rev. Phys.* **1** 731
[3] Kasevich M and Chu S 1991 Atomic interferometry using stimulated Raman transitions *Phys. Rev. Lett.* **67** 181
[4] Peters A, Chung K Y and Chu S 2001 High-precision gravity measurements using atom interferometry *Metrologia* **38** 25
[5] Altin P A *et al* 2013 Precision atomic gravimeter based on Bragg diffraction *New J. Phys.* **15** 023009
[6] McGuirk J M, Foster G T, Fixler J B, Snadden M J and Kasevich M A 2002 Sensitive absolute-gravity gradiometry using atom interferometry *Phys. Rev.* A **65** 033608
[7] Lamporesi G, Bertoldi A, Cacciapuoti L, Prevedelli M and Tino G M 2008 Determination of the Newtonian gravitational constant using atom interferometry *Phys. Rev. Lett.* **100** 050801
[8] Rudolph J, Wilkason T, Nantel M, Swan H, Holland C M, Jiang Y, Garber B E, Carman S P and Hogan J M 2020 Large momentum transfer clock atom interferometry on the 689 nm intercombination line of strontium *Phys. Rev. Lett.* **124** 083604
[9] Cheiney P, Fouché L, Templier S, Napolitano F, Battelier B, Bouyer P and Barrett B 2018 Navigation-compatible hybrid quantum accelerometer using a Kalman filter *Phys. Rev. Appl.* **10** 034030
[10] Gustavson T L, Bouyer P and Kasevich M A 1997 Precision rotation measurements with an atom interferometer gyroscope *Phys. Rev. Lett.* **78** 2046
[11] Barrett B, Geiger R, Dutta I, Meunier M, Canuel B, Gauguet A, Bouyer P and Landragin A 2014 The Sagnac effect: 20 years of development in matter-wave interferometry *C. R. Phys.* **15** 875
[12] Hoth G W, Pelle B, Riedl S, Kitching J and Donley E A 2016 Point source atom interferometry with a cloud of finite size *Appl. Phys. Lett.* **109** 071113
[13] Moler K, Weiss D S, Kasevich M and Chu S 1992 Theoretical analysis of velocity-selective Raman transitions *Phys. Rev.* A **45** 342
[14] Müller H, Chiow S-w, Long Q, Herrmann S and Chu S 2008 Atom interferometry with up to 24-photon-momentum-transfer beam splitters *Phys. Rev. Lett.* **100** 180405
[15] Müller H, Chiow S-w and Chu S 2008 Atom-wave diffraction between the Raman–Nath and the Bragg regime: effective Rabi frequency, losses, and phase shifts *Phys. Rev.* A **77** 023609
[16] Szigeti S S, Debs J E, Hope J J, Robins N P and Close J D 2012 Why momentum width matters for atom interferometry with Bragg pulses *New J. Phys.* **14** 023009
[17] Hartmann S, Jenewein J, Giese E, Abend S, Roura A, Rasel E M and Schleich W P 2020 Regimes of atomic diffraction: Raman versus Bragg diffraction in retroreflective geometries *Phys. Rev.* A **101** 053610

J. Phys. B: At. Mol. Opt. Phys. **55** (2022) 205501

J Saywell *et al*

[18] As the output of a Bragg interferometer is the phase of a momentum superposition, the read-out time must be long enough for this to produce a detectable spatial separation.

[19] Lévèque T, Gauguet A, Michaud F, Pereira Dos Santos F and Landragin A 2009 Enhancing the area of a Raman atom interferometer using a versatile double-diffraction technique *Phys. Rev. Lett.* **103** 080405

[20] Malossi N, Bodart Q, Merlet S, Lévèque T, Landragin A and Santos F P D 2010 Double diffraction in an atomic gravimeter *Phys. Rev.* A **81** 013617

[21] He M, Chen X, Fang J, Ge G, Li J, Zhang D, Zhou L, Wang J and Zhan M 2021 Phase shift of double-diffraction Raman interference due to high-order diffraction states *Phys. Rev.* A **103** 063310

[22] Berg P, Abend S, Tackmann G, Schubert C, Giese E, Schleich W P, Narducci F A, Ertmer W and Rasel E M 2015 Composite-light-pulse technique for high-precision atom interferometry *Phys. Rev. Lett.* **114** 063002

[23] Skinner T E, Reiss T O, Luy B, Khaneja N and Glaser S J 2003 Application of optimal control theory to the design of broadband excitation pulses for high-resolution NMR *J. Magn. Reson.* **163** 8

[24] Khaneja N, Reiss T, Kehlet C, Schulte-Herbrüggen T and Glaser S J 2005 Optimal control of coupled spin dynamics: design of NMR pulse sequences by gradient ascent algorithms *J. Magn. Reson.* **172** 296

[25] Glaser S J *et al* 2015 Training Schrödinger's cat: quantum optimal control *Eur. Phys. J.* D **69** 279

[26] Doria P, Calarco T and Montangero S 2011 Optimal control technique for many-body quantum dynamics *Phys. Rev. Lett.* **106** 190501

[27] Brif C, Chakrabarti R and Rabitz H 2010 Control of quantum phenomena: past, present and future *New J. Phys.* **12** 075008

[28] Eitan R, Mundt M and Tannor D J 2011 Optimal control with accelerated convergence: combining the Krotov and quasi-Newton methods *Phys. Rev.* A **83** 053426

[29] Machnes S, Assémat E, Tannor D and Wilhelm F K 2018 Tunable, flexible, and efficient optimization of control pulses for practical qubits *Phys. Rev. Lett.* **120** 150401

[30] Janich M A, Schulte R F, Schwaiger M and Glaser S J 2011 Robust slice-selective broadband refocusing pulses *J. Magn. Reson.* **213** 126

[31] Kobzar K, Skinner T E, Khaneja N, Glaser S J and Luy B 2004 Exploring the limits of broadband excitation and inversion pulses *J. Magn. Reson.* **170** 236

[32] Saywell J C, Kuprov I, Goodwin D, Carey M and Freegarde T 2018 Optimal control of mirror pulses for cold-atom interferometry *Phys. Rev.* A **98** 023625

[33] Saywell J, Carey M, Belal M, Kuprov I and Freegarde T 2020 Optimal control of Raman pulse sequences for atom interferometry *J. Phys. B: At. Mol. Opt. Phys.* **53** 085006

[34] Saywell J, Carey M, Kuprov I and Freegarde T 2020 Biselective pulses for large-area atom interferometry *Phys. Rev.* A **101** 063625

[35] Saywell J, Carey M, Dedes N, Kuprov I and Freegarde T 2021 Can optimised pulses improve the sensitivity of atom interferometers? *Proc. SPIE 11881, Quantum Technology: Driving Commercialisation of an Enabling Science II* p 118810

[36] McGuirk J M, Snadden M J and Kasevich M A 2000 Large area light-pulse atom interferometry *Phys. Rev. Lett.* **85** 4498

[37] Weiss D S, Young B C and Chu S 1993 Precision measurement of the photon recoil of an atom using atomic interferometry *Phys. Rev. Lett.* **70** 2706

[38] For an atom initially in $|g_0\rangle$ the atom will be in the internal state $|g\rangle$ ($|e\rangle$) after receiving an even (odd) number of two-photon recoil shifts, where the dimension of the state space grows by 2 following each wave-vector reversal.

[39] This problem does not arise in conventional Raman interferometers as the atoms are placed into a superposition of different internal states, which enables them to remain distinguishable regardless of the momentum width.

[40] Goodwin D L 2018 Advanced optimal control methods for spin systems *PhD Thesis* University of Southampton

[41] Kobzar K, Ehni S, Skinner T E, Glaser S J and Luy B 2012 Exploring the limits of broadband 90° and 180° universal rotation pulses *J. Magn. Reson.* **225** 142

[42] De Fouquieres P, Schirmer S G, Glaser S J and Kuprov I 2011 Second order gradient ascent pulse engineering *J. Magn. Reson.* **212** 412

[43] Goodwin D L and Kuprov I 2016 Modified Newton–Raphson GRAPE methods for optimal control of spin systems *J. Chem. Phys.* **144** 204107

[44] Nocedal J and Wright S J 2006 *Numerical Optimization* (New York: Springer)

[45] Luy B, Kobzar K, Skinner T E, Khaneja N and Glaser S J 2005 Construction of universal rotations from point-to-point transformations *J. Magn. Reson.* **176** 179

[46] Physically, this error arises from variations in laser intensity experienced by the atom that are constant during the pulse but which vary from pulse-to-pulse and/or from variations that are constant in time over the whole sequence but which vary spatially across the atom cloud.

[47] In practice, it takes a finite time to switch the direction of the effective wave-vector. We find that introducing equal delays between the individual pulses does not affect the pulse performance in the simulations, only the superposition phase introduced by the beamsplitter sequences.

[48] Hogben H J, Krzystyniak M, Charnock G T P, Hore P J and Kuprov I 2011 Spinach—a software library for simulation of spin dynamics in large spin systems *J. Magn. Reson.* **208** 179

[49] Stammers J 2019 An atom interferometer for measuring horizontal accelerations *PhD Thesis* Imperial College London

[50] Sugarbaker A 2014 Atom interferometry in a 10 M fountain *PhD Thesis* Stanford University

[51] Gillot P, Cheng B, Merlet S and Pereira Dos Santos F 2016 Limits to the symmetry of a Mach–Zehnder-type atom interferometer *Phys. Rev.* A **93** 013609

[52] Freegarde T and Segal D 2003 Algorithmic cooling in a momentum state quantum computer *Phys. Rev. Lett.* **91** 037904

[53] Giese E 2015 Mechanisms of matter-wave diffraction and their application to interferometers *Fortschr. Phys.* **63** 337